Thermal Dissociation of Compressed ZnO and SnO_2 Powders in a Moving-Front Solar Thermochemical Reactor

Marc Chambon, Stéphane Abanades, and Gilles Flamant
Processes, Materials and Solar Energy Laboratory (CNRS-PROMES), 66120 Font-Romeu, France

DOI 10.1002/aic.12432
Published online November 2, 2010 in Wiley Online Library (wileyonlinelibrary.com).

The high-temperature thermal dissociation reaction of ZnO and SnO_2 was investigated, as part of a two-step thermochemical water-splitting cycle for H_2 production. A lab-scale solar reactor (1 kW) was designed, built, and operated for continuous dissociation of volatile oxides under reduced pressure. In this reactor, compressed oxide powders placed in a vertical ceramic cavity are irradiated by highly concentrated solar energy. The reactor design allows moving the reaction front for achieving continuous reactant feeding. ZnO and SnO_2 thermal dissociations were successfully performed at about 1900 K, with the recovery of up to 50% of products as nanopowders with high specific surface area (in the range 20–60 m^2/g) and with mass fractions of reduced species up to 48 wt % for Zn and 72 wt % for SnO. The performed O_2 measurements confirmed the kinetics of ZnO dissociation and gave an activation energy of 380 ± 16 kJ/mol, based on an ablation regime of the ZnO surface. © 2010 American Institute of Chemical Engineers *AIChE J*, 57: 2264–2273, 2011

Keywords: thermochemical cycles, zinc, tin oxide, dissociation, solar reactor, kinetics

Introduction

Two-step thermochemical cycles (TC)[1] have the potential for high solar-to-hydrogen energy conversions and should be more efficient than water electrolysis from solar thermal electricity (25% for solar-to-electricity efficiency and 80% for electrolysis efficiency).[2,3] These TCs are made possible by the high temperatures (above 1000 K) provided by solar concentrating systems,[4] and are tradeoffs in both simplicity and technical bottlenecks between low temperature TCs (below 1200 K but more steps) and direct water thermolysis (above 3000 K).[5,6] Most of two-step TCs consist of redox reactions based on M_xO_y/M_xO_{y-1} redox pairs, enabling separate production of hydrogen and oxygen from water as follows:

High - temperature reduction (solar) :

$$M_xO_y \rightarrow M_xO_{y-1} + \tfrac{1}{2}O_2 \quad \text{(endothermal)} \quad (1)$$

Low - temperature water - splitting :

$$M_xO_{y-1} + H_2O \rightarrow M_xO_y + H_2 \quad \text{(exothermal)} \quad (2)$$

Previous studies showed that ZnO is a promising candidate oxide owing to its relatively low reduction temperature (below 2200 K).[7] In addition, large amounts of H_2 can be generated from the produced Zn (equivalent to a 3 wt % H_2 storage) and rapid kinetics for the water-splitting step was observed (Zn hydrolysis below 700 K).[2,8,9] Pending issues are related to the design of the concentrating system for reaching the operating temperature, the required refractory materials for the solar reactor (availability, cost, resistance to chemical products, and thermal shocks),[5] and the recombination reaction occurring in the cooling zone of the solar reactor output. Indeed, the ZnO dissociation yields O_2 and Zn vapor in the gas phase, and quenching via neutral gas is

Correspondence concerning this article should be addressed to S. Abanades at abanades@promes.cnrs.fr.

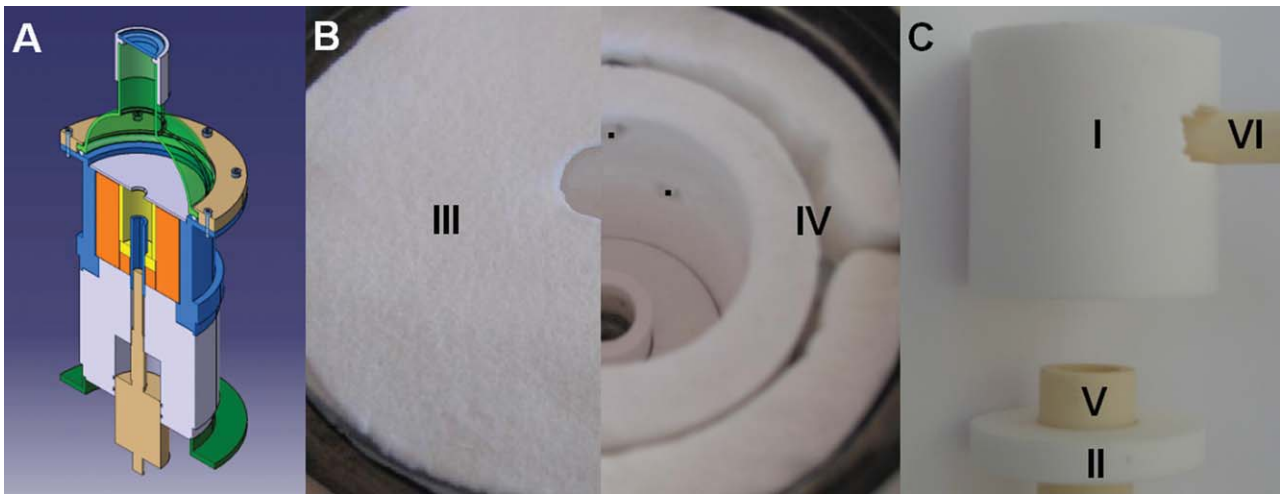

Figure 1. A: Simplified cross section of the reactor (gas input/output not represented), B: Insulation: composite view with and without the diaphragm (black dots: thermocouples) C: Refractory parts: alumina parts layout (capillary for auxiliary gas input not represented).

[Color figure can be viewed in the online issue, which is available at wileyonlinelibrary.com.]

required to limit the parasitic oxidation thermodynamically favored at the solar reactor output,[10]

Recombination :

$$M_xO_{y-1} + \tfrac{1}{2}O_2 \rightarrow M_xO_y \qquad \text{(exothermal)} \quad (3)$$

Recently, two other similar TCs based on the SnO_2/SnO[11] and GeO_2/GeO redox pairs[12] were experimentally validated. Concerning the solar reactor engineering, researches have been developed for ZnO dissociation with either directly (cavity-type filled with ZnO)[13–15] or indirectly (ZnO aerosols flowing through opaque tubes) irradiated reactors.[16] Indirect heating is attractive due to the elimination of the window separating the reactants from the atmosphere, but the material choice is restricted. As an example, graphite or silicon carbide materials provide a fast enough solar heat transfer inside the opaque tubes,[17] but do not resist to oxidation at these very high temperatures and the use of a fluid-wall reactor would hardly be sufficient to protect oxidation-sensitive boundaries.[18] A lab-scale cavity-type reactor (1 kW) was previously designed, built, and operated for continuous solar thermal dissociation of volatile oxides under reduced pressure.[19] Low pressures help to improve the dissociation rate and to decrease the recombination rate via a low O_2 partial pressure (Le Chatelier's principle). Extra pumping work can be justified by the diminution of the dissociation temperature, which decreases (1) thermal losses (especially radiative losses), (2) neutral gas requirements for a given recombination rate, and (3) capital costs due to the use of standard refractory materials (pure sintered alumina below 2073 K).[20] ZnO powder was fed in the rotary reactor thanks to a screw inserted in an alumina tube. The powder reacted on the hot walls, and product gases were flushed via neutral gas injected from the cavity aperture. Finally, the condensed species (Zn solar-powder) was collected on a ceramic filter. It was possible to perform more than a dozen of solar tests with the same refractory materials. However, this reactor entailed several drawbacks such as (1) the lack of accurate measurements because the cavity rotation prevents the use of thermocouples and the residual air leakages at the sealing of the rotary components (due to low pressures) make the O_2 monitoring difficult; (2) the low recovery yield of reduced particles at the filter (max. 21%) due to the long path between the reactor cavity output and the filter, promoting deposition on the walls; and (3) the low efficiency because of heat losses (mostly at the copper plate front face and water-cooled reactor walls according to a numerical simulation[21]). The first issue makes this reactor irrelevant for detailed characterization, while the other ones make subsequent tests difficult (water-splitting, powder characterizations) due to small quantities of solar-produced powder.

The goal of this study was to design and qualify a novel and more efficient solar reactor suitable for the SnO_2/SnO and ZnO/Zn TCs. First, the study on this new reactor aimed at collecting more data (temperature and O_2 concentration measurements) for SnO_2 and ZnO dissociations to determine the chemical and thermochemical performances, and to analyze the kinetics of the reduction. In addition, there was a need for producing significant and representative amounts of reduced species (solar-produced SnO and Zn) for hydrolysis tests and morphological characterizations (XRD, SEM, BET). This article details the design and the performance evaluation results pertaining to the novel solar reactor concept for ZnO and SnO_2 thermal dissociation.

Solar Reactor Design

The drawbacks of the previously developed reactor[19] were respectively corrected by (1) eliminating the rotation of the cavity to avoid the air leakage issue at low pressure, (2) implementing a short straight path for the hot product gases from the reactor output to the filter, and (3) using a refractory aperture and an insulated ceramic cavity. The developed solar reactor was composed of a Pyrex™ window and a cylindrical, water-cooled reactor shell (depth: 76 mm, diameter: 88 mm) made of stainless steel (Figure 1A). The cavity materials consisted of pure sintered alumina (Degussit™

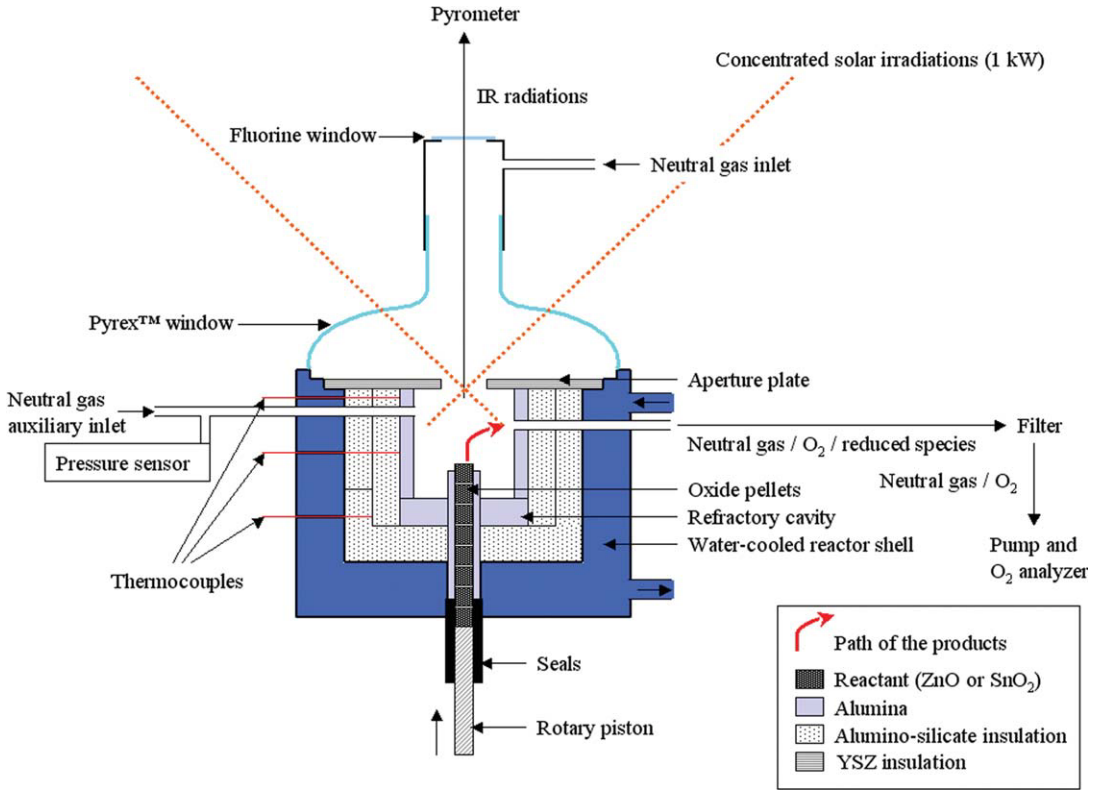

Figure 2. Experimental setup for the solar thermal dissociation of ZnO or SnO_2.

[Color figure can be viewed in the online issue, which is available at wileyonlinelibrary.com.]

AL23, $T_{max} = 2223$ K) for the tubes and plates, zirconia felt for the aperture plate (yttria-stabilized zirconia fibers, Zircar™ ZYF-50, thickness: 1.3 ± 0.4 mm, $T_{max} = 3223$ K) and alumino-silicate for the insulation (Promat™ Promaform 1600, $T_{max} = 1873$ K). They were qualified in a previous study[19] with respect to chemical and thermal stability.[22] The refractory cavity (Figures 1B, C) was composed of a 30 mm-long alumina tube (30 mm i.d., 4 mm-thick) with gas input/output bored via a diamond saw (I), closed at the bottom by a 7 mm-thick and 37 mm-diameter cylindrical plate (with a centered 15.5 mm i.d. hole) (II) and at the top by a 3 mm-thick aperture plate (88 mm o.d., 12 mm-diameter aperture) made of two layers of zirconia felt (III). This set of refractory parts was inserted into a modular insulation filling the inside of the reactor body (IV). The reactant consisted of 3–8 mm-thick pellets (8 mm-diameter) brought forth by compressing up to 2 g of commercial oxide powder (SnO_2 or ZnO, Prolabo™, mean diameter of about one micron, purity above 99%). They were stacked in a 60 mm-long alumina feeding tube (10 mm i.d., 15 mm o.d.) exceeding of 7 mm the bottom of the refractory cavity (V). This pile of pellets formed an oxide "rod" that was pushed upward via a screw piston manually rotated for achieving a continuous reactant injection during an experimental run. Both the powders and the insulation were preliminarily calcined during 5 h at 1073 K to eliminate impurities and organic traces (organic binders) that could hinder O_2 measurements. Neutral gas (N_2 or Ar) was introduced via the aperture to protect the glass window from the convective flow of product gases (Figure 2). Additional inert carrier gas was also optionally injected from an inlet port located at the upper side of the cavity (3 mm i.d. tube), also connected to a pressure sensor (Pfeiffer Vacuum™ PCR260 capacitance gauge) to measure the operating pressure inside the cavity. Gas flowrates were regulated with mass-flow controllers (Brooks™ calibrated with N_2, precision: 0.7 ± 0.2% of the full scale, scale: 0–5 NL/min). Although a gas preheater was not directly implemented in this reactor,[13] the hot aperture plate (heated by the solar irradiation fraction that does not enter the cavity and by inside IR radiation from the cavity) acts as a gas preheater. The inert carrier gas and gas products (O_2 and reduced species) exit the cavity via an outlet tube at the opposite side of the cavity (VI). This outlet tube was a 15-cm long alumina tube (5 mm i.d. and 6 mm o.d.) that was used to avoid direct contact between the hot gases and the cold walls. Indeed, condensation of $Zn_{(g)}$ or $SnO_{(g)}$ vapors on water-cooled walls can be responsible for significant deposits. At larger scale, this can be limited via an annular flow of neutral gas at the reactor output, also used for quenching.[10] Then the condensed species were carried up to a specific nanoparticle filter located 20 cm downstream (CTI™, $T_{max} = 1523$ K, porous tube made in alumina with seven inner canals for minimized pressure drop, covered with ultrapure TiO_2 nanoparticles for improved filtration, surface: 22.7×10^{-3} m^2).

Experimental Setup and Methods

The reactor was installed at the focus of a vertical axis solar furnace composed of a sun-tracking heliostat reflecting vertically the solar irradiation toward a facedown concentrator. The concentrator consisted of a parabola (2 m-diameter,

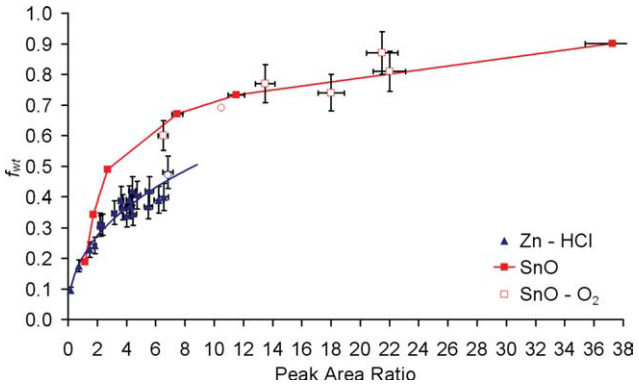

Figure 3. Calibration curves used for XRD powders analysis after ZnO or SnO_2 dissociation; (o) thermogravimetric references.

[Color figure can be viewed in the online issue, which is available at wileyonlinelibrary.com.]

0.85 m-focal distance) similar to the ones used with previous reactors.[19] It was fixed above the reactor frame, concentrating the incident solar irradiation coming from the heliostat on the focal point (Figure 2). The total power of this concentrator, measured with a diffusing plate shot by a CCD camera (calibration done by calorimetry), was 1.4 ± 0.1 kW for a direct normal irradiation (DNI) of 1 kW/m^2. As the concentrated solar flux density shows a Gaussian distribution profile with a maximum concentration ratio C of 16,000, the power absorbed by the cavity through the 12-mm diameter aperture is 1050 ± 80 W.[21] Four temperature measurements were performed. Two sensors measured the temperature at the cavity external walls (B-thermocouples in contact with the top and middle of the alumina tube, 14 ± 2 mm in between) and one sensor inside the insulation (K-type thermocouple at 13–15 mm far from the cold walls and at the bottom of the cavity level). Finally, a solar-blind pyrometer (Heitronics^{TM} KT15 at 5.2 μm) measured directly the temperature of the upcoming oxide inside the cavity through a fluorine window (Figure 2). This device, previously calibrated with a blackbody, was assumed to give the real temperature based on the reactor type (cavity) and on the wall average emissivity near to unity (0.9 for alumina above 4.5 μm leading to a temperature underestimation below 3%, i.e. 60 K).[23] Continuous O_2 measurements were performed on-line via gas sampling at the filter output and analysis with a zirconia probe (Setnag^{TM} JC48V, range: 10–10000 ppm, precision: 0.2%, calibration with 5040 ppm O_2 in N_2). Temperatures and O_2 concentration data were monitored and numerically recorded for subsequent exploitations, while the pressure and the rod elevation (2 mm per revolution of the rotary piston) were noted relatively.

In addition to the operating parameters (temperature, flow-rates, pressure) and O_2 measurements, a key parameter for reactor performance evaluation was the mass fraction of reduced species in the solar-produced powder f_{wt} (yield of the dissociation reaction):

$$f_{wt} = \frac{m_{red}}{m_{red} + m_{ox}} \quad (4)$$

It was estimated via a nondestructive internal calibration method based on X-ray diffractometry [Philips^{TM} PW 1820 with CuKα source (0.154 nm)].[24] The area ratios of the primary XRD peak of the reduced species (43.2° for Zn and 29.9° for SnO) to a well-identified peak of the oxide (31.7° for ZnO and 26.6° for SnO_2) were plotted as a function of f_{wt}. Consequently, the resulting calibration curves (Figure 3) allowed direct estimation of the dissociation yields from XRD patterns of unknown samples. This method was reliable and convenient for fast quantitative analysis. Each standard sample was prepared by blending the commercial oxide with pure powder of reduced species obtained from solar ferro-reduction (FeO used as a reducing compound). This calibration was validated by an oxygen mole balance during SnO_2 dissociation[25] (Figure 3, SnO–O_2). In the case of solar-produced Zn powders, the dissociation yields were quantified by measuring the amount of hydrogen released via complete dissolution of a sample (about 200 mg) in a concentrated aqueous solution of hydrochloric acid (10 wt %), yielding hydrogen in a quantitative way (Figure 3, Zn–HCl). In addition, a reference data (Figure 3, circles) was also used for Zn and SnO (thermogravimetric analysis of a complete oxidation) to determine the method uncertainties (±5% relative). Finally, crystallite sizes were estimated with the Scherrer equation.[26]

This procedure was applied to analyze separately the different samples collected in each deposition zone: (A) deposit in the output alumina tube VI, (B) deposit on the walls between the output tube and the filter, (C) deposit on the filter (Figure 4). The oxide pellets and output tube were weighted prior to each test to deduce the mass variations after the experiments. Hard deposits in the output alumina tube after operation were removed via dissolution in diluted acetic acid.

Finally, morphological analysis of the recovered powders was performed via scanning electron microscopy (Hitachi^{TM} S-4500) and N_2 adsorption/desorption for specific surface area characterization via manometry (Micromeritics^{TM} ASAP 2010, preliminary desorption at 573 K).

Experimental Results and Discussion

Solar thermal dissociations

The reactor was operated for DNI (Direct Normal Irradiation) above 900 W/m^2 at cavity pressures in the range 15–77 kPa and neutral gas flow-rates in the range 3–6.5 NL/min. Prior to the first operation, the reactor was heated over 1273 K without any window to eliminate residual hydrocarbons. The feeding tube was fully loaded with about 10 oxide

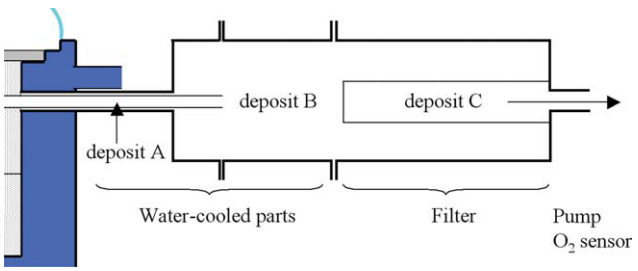

Figure 4. Reactor output zones where the condensed reduced species are collected.

[Color figure can be viewed in the online issue, which is available at wileyonlinelibrary.com.]

Table 1. Summary of the Solar Tests: Thermal Behavior with Maximum Temperatures

Run No.	DNI W/m^2	Neutral Gas Flow-Rate (NL/min)	P (kPa)	Time to Reach Thermal Equilibrium (min)	Equilibrium Duration Δt (min)	$T_{insulation}$ (K)	T_{cavity}, middle (K)	T_{cavity}, top (K)	$T_{pyrometer}$ (K)
1	900	5	20	16	10	893	1183	1353	1833
2	950	4	17.5	15	10	1183	1543	1663	1883
3	900	3	14	15	11	983	1283	1433	1753
4	950	5*	19	16	3	813	1043	1203	1873
5	900	5*	19.5	20	19	1193	1523	1673	1903
6	900	4	17.5	14	22	1103	1413	1573	1843
7	900	6.5 (Ar)*	28.5	18	16	843	1363	1443	1913
8	1000	4.9 (Ar)	77	13	12	953	1643	1733	1943
9	900	4	15	20	3	743	1133	1243	1713
10	1000	4	19	13	17	1033	1563	1673	1913
11	900	4	17.5	16	13	1233	1743	1763	1893
12	900	5	20.5	16	22	933	1283	1313	1713
13	950	4	18	12	26	1133	1583	1653	1873
14	1000	4	19	10	24	1183	1643	1698	1893
15	950	4.2 (Ar)	22	12	14	1293	1763	1846	1959
16	900	4	16	16	18	1213	1703	1703	1993
17	950	4	16	12	16	1268	1763	1813	1913
18	950	5	19.5	9	22	1203	1663	1703	1868
Average	925	4.3	22	15	15	1065	1490	1580	1870

Tests were thermal dissociations of ZnO, except for runs #16–18 (SnO_2). If not stated, neutral gas was N_2. Pressure is an average value (±20% variation, pressure drop caused by the growing deposit on the filter). Δt was taken as the time corresponding to a pyrometer temperature above 1663K.
*Tests with auxiliary gas injection (20% of the total neutral gas flow-rate).

pellets (reactant height: 60 mm, reactant at the level of the alumina feeding tube tip, see Figure 2) before each test to allow a pseudo-continuous process and to protect the piston at the bottom from high temperatures. Then, the reactor was flushed twice with neutral gas, resulting in O_2 traces below 140 ppm at the filter output (residual O_2 traces for $P = 20$ kPa and 4 NL/min N_2).

Results concerning the thermal behavior of this reactor are summed up in Table 1. Thermal equilibrium was reached after about 15 min for all the tests, with an equilibrium temperature around 1000 K in the center of the insulation layer. The reactor temperature was also significantly below the alumina melting point. Thermal gradients in the alumina tube (cavity) were estimated to be 7 000 and 70 000 K/m axially and radially, respectively. No significant effect of the neutral gas (N_2 or Ar) on the thermal behavior was noticed.

Effect of the flow conditions on the thermal behavior of the reactor was hardly visible because of the small variations imposed. Nevertheless, the time to reach thermal equilibrium was shown to decrease with the gas residence time, which is inversely proportional to the factor $B = F_{N2}/P$ (Figure 5). Indeed, the residence time is inversely proportional to the volumetric gas flow-rate (thus to B factor) at constant reactor volume and temperature. Figure 5 shows that the time to reach thermal equilibrium increases with B factor. The lower the residence time, the higher the convective heat losses, and thus thermal equilibrium is postponed. However, this may not be true if pressures are significantly different. Although a low pressure increases the convective losses by decreasing the residence time, on the contrary it decreases the conductive losses in the insulation (open porosity).

Observation of the refractory parts after the runs showed that the reactor was even more robust than the previous one.[19] Only the alumina parts I and II showed minor cracks after a dozen of tests above 1673 K (axial for part I, radial for part II), which did not prevent additional solar runs. Prior to O_2 quantitative analysis, semiquantitative gas chromatography showed that reducing gases (H_2 and hydrocarbon compounds, assumed to come from the sealing and insulation materials) were negligible.

Dissociation was proven to start at about 1663 K (for a pressure around 20 kPa) for both ZnO and SnO_2 due to concomitant O_2 increase and visible particles deposition on the filter (transparent encapsulation) (Figures 6 and 7). The residence time between the reactor and the filter output was taken into account for synchronizing the measurements, since a delay of 5 ± 1 s (20 kPa, 4 NL/min N_2) was observed between a moving up of the reactant rod and the resulting O_2 concentration increase. Assuming that the dissociation occurs only above 1663 K, its duration Δt was inferred for each test. After each solar dissociation, the product species were collected at the reactor output (Figure 4).

The deposit A could hardly be fully recovered (hard deposit) and thus, its mass was deduced by weighting the outlet tube VI before and after the test. This deposit showed only a residual fraction of reduced species (below 10 wt %). Indeed, the hot vapors of reduced species significantly

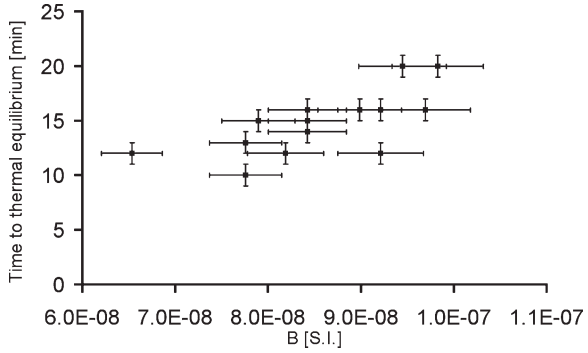

Figure 5. Variation of the time to reach thermal equilibrium as a function of the N_2 flow-rate to pressure ratio (B).

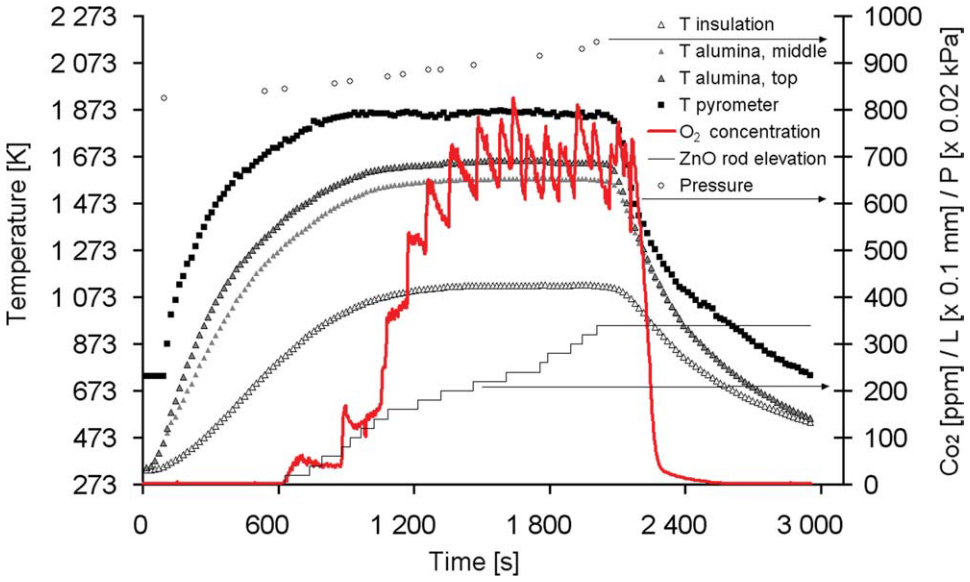

Figure 6. Measurements for the solar dissociation of ZnO (run #13), no injection at the auxiliary gas inlet.

Shutter fully opened at time zero and closed at 2150 s. [Color figure can be viewed in the online issue, which is available at wileyonlinelibrary.com.]

condensed in the outlet alumina tube, and both high temperatures and O_2 presence favored the recombination reaction. Inversely, deposits B and C consisted of powders with a high fraction of reduced species, which was enhanced by deposit A acting as an O_2 scavenger for the sake of the remaining reduced species. Up to 50% of the products was recovered as nanopowders (deposits B and C) and the yield of particle recovery in the filter (deposit C) was up to 31% (max 21% in the previous reactor[19]). The amounts of the powder deposits are summed up in Figure 8.

Deposit A was omitted during the first tests (#1–6). Tests with low product collection (#1,4,9) could be explained by the significantly lower cavity temperatures. The reactor heating was less efficient in these tests because of the broadening of the aperture diameter, thereby increasing the radiative losses. Indeed, the zirconia felt (used as the aperture plate) partially melt due to a high solar flux irradiation at the focal zone and to the presence of hot spots (nonsymmetrical flux distribution at the focus). For the other tests, at least 1 g of reduced species was collected for a dissociation duration Δt (equivalent to the thermal equilibrium time). About half of the total amount of product was recovered as deposit A and the remaining part was found as a valuable reactive powder (deposits B and C) for subsequent characterization. A high

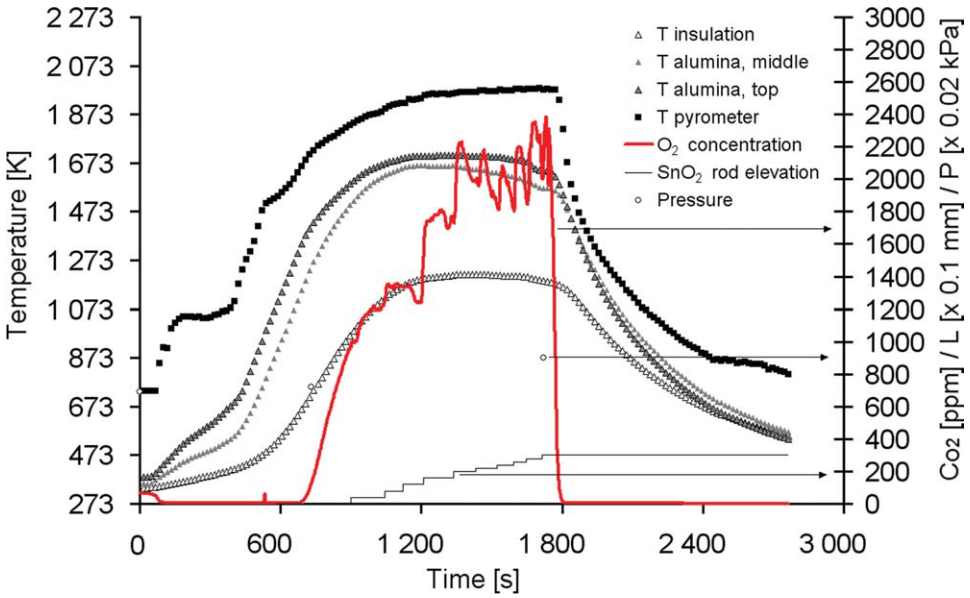

Figure 7. Measurements for the solar dissociation of SnO_2 (Run #16), no injection at the auxiliary gas inlet.

Shutter fully opened at time zero and closed at 1750 s. [Color figure can be viewed in the online issue, which is available at wileyonlinelibrary.com.]

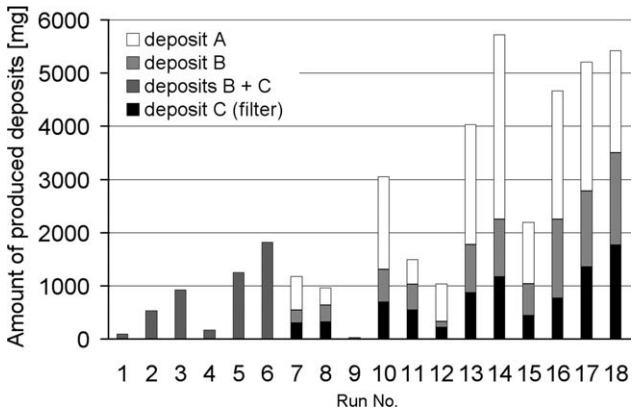

Figure 8. Amounts of powder deposits collected in each zone of the reactor output.

For tests #1–6 and 9, deposits B and C were mixed before weighting. Runs 1–15: ZnO dissociation, runs #16–18: SnO_2 dissociation.

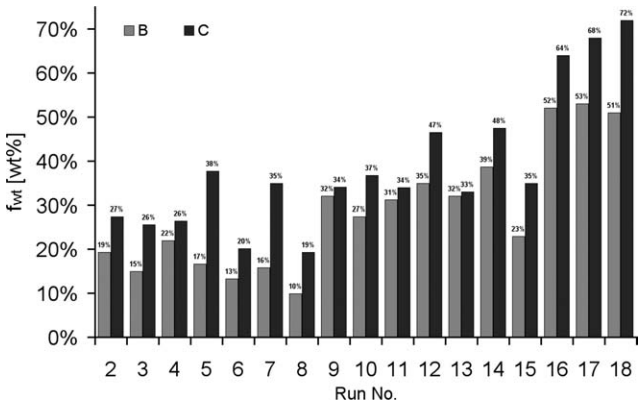

Figure 9. Weight fractions of reduced species estimated by XRD for the powders collected in the zones B and C (filter).

neutral gas flow-rate can limit the amount of deposit A via a decreased residence time in tube VI, but this may lead to the reactor cooling (trend observed in Figure 5 representing the time to reach thermal equilibrium as a function of a variable proportional to the neutral gas flow-rate), and thus to a decreased reactor efficiency.

A possible solution could consist in decreasing the length of tube VI and promoting product gas cooling via a new neutral gas input set perpendicularly to the output of this tube as proposed in Ref. [10] for efficient quenching via a turbulent flow. However, deposit A seems to be unavoidable since even gas sheathing does not prevent the reduced species vapor from diffusing up to the walls.[18]

Figure 9 shows the weight fractions of reduced species determined by the XRD method for the deposits B and C (filter). The fractions for deposit C were typically higher than the fractions for deposit B. In addition, the mass fractions of reduced species in the synthesized SnO powders (maximum 72%) were always higher compared to Zn in similar conditions. This means that the recombination reaction is less favored in the case of SnO, as evidenced in a previous study on the recombination rate characterization.[25] The overall weight fraction of reduced species in the product was estimated from:

$$\overline{f_{\mathrm{wt}}} = \sum_n w_{\mathrm{n}} f_{\mathrm{wt},n} \tag{5}$$

where n defines the sample (deposit A, B or C) and w_{n} the mass fraction of sample n.

The total mass of products m_{p} (Figure 8) or the pellet mass variation when available (runs #11–18) were used to estimate the mean molar flow-rate of reduced species at the surface of the decomposing oxide:

$$\overline{F_{\mathrm{red}}} = \left(\frac{\overline{f_{\mathrm{wt}}}}{M_{\mathrm{red}}} + \frac{1-\overline{f_{\mathrm{wt}}}}{M_{\mathrm{ox}}}\right)\frac{m_{\mathrm{p}}}{\Delta t} = \frac{\Delta m_{\mathrm{ox}}}{M_{\mathrm{ox}}\cdot\Delta t} \tag{6}$$

Consequently, the dilution ratio d was estimated from:

$$d = \frac{F_{\mathrm{ng}} + 1.5\cdot\overline{F_{\mathrm{red}}}}{1.5\cdot\overline{F_{\mathrm{red}}}} \tag{7}$$

where F_{ng} stands for the neutral gas flow-rate.

The filtration pressure drop was quantified in a normalized way as:

$$npd = \left(\frac{\Delta P}{\overline{P}}\Big/ m_c\right)S \tag{8}$$

where ΔP is the pressure variation during the solar test, m_{c} the mass of powder collected on the filter and S the filter area. Finally, the global selectivity of the solar reactor (mean mole fraction of reduced species in the final product, $\overline{f_{\mathrm{mol}}}$, equal to unity if no recombination occurs) was expressed as:

$$\overline{f_{\mathrm{mol}}} = \frac{\overline{f_{\mathrm{wt}}}}{M_{\mathrm{red}}}\Big/\left(\frac{\overline{f_{\mathrm{wt}}}}{M_{\mathrm{red}}} + \frac{1-\overline{f_{\mathrm{wt}}}}{M_{\mathrm{ox}}}\right) \tag{9}$$

The thermochemical efficiency of the reactor was estimated as:

Table 2. Summary of the Data for the Solar Dissociations [ZnO, except for Runs #16–18 (SnO_2)]

Run No.	2	3	4	5	6	7	8	10	11	12	13	14	15	16	17	18
d	<170	<90	<180	<180	<120	<210	<150	<50	40	210	57	36	52	65	52	76
Npd (m^2/kg)	12.2	4.6	16.2	7.1	6.2	9.9	0.8	7.5	3.0	6.7	3.2	3.4	8.3	7.8	7.6	3.4
Q (W)	998	945	998	945	945	945	1050	1050	945	945	998	1050	998	945	998	998
$\overline{F_{\mathrm{red}}}$ (mmol/min)	0.73	1.08	0.86	0.85	1.08	0.94	1.02	2.59	3.05	0.71	2.11	3.40	2.28	1.81	2.59	2.00
$\overline{f_{\mathrm{mol}}}$ (%)	<28	<21	<26	<23	<18	<17	<13	19	28	17	18	22	18	34	36	40
η (%)	0.7<	1.0<	0.8<	0.8<	1.0<	0.9	0.9<	2.2	2.9	0.7	1.9	2.9	2.1	2.2	2.9	2.4

Neutral gas was N_2 except for runs #7–8 and 15 (Ar). Pressure was about 20 kPa, except for run #8 (77 kPa). Typical relative uncertainties were 5% for d, and 20–30% for $\overline{f_{\mathrm{mol}}}$ and η (5% for Δt, 10% for f_{wt}, 5% for Q).

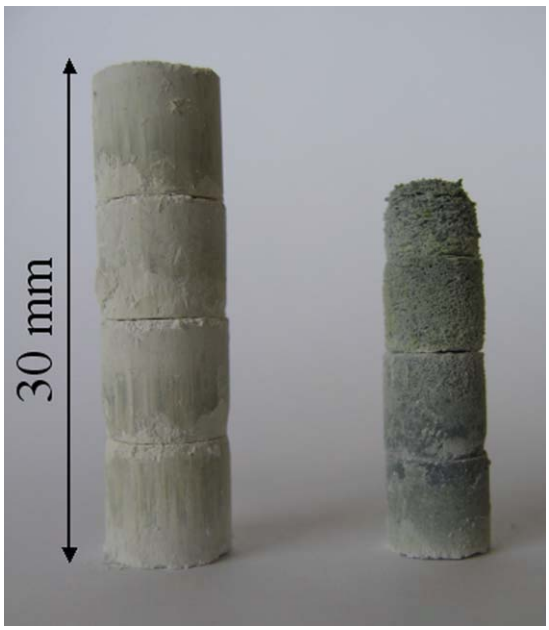

Figure 10. Photograph of ZnO oxide pellets before (left) and after (right) high-temperature heating in the solar reactor.

The topmost pellet on the right is partially consumed. [Color figure can be viewed in the online issue, which is available at wileyonlinelibrary.com.]

$$\eta = \frac{\overline{F_{\text{red}}} \cdot \Delta H}{Q} \tag{10}$$

where ΔH is the required enthalpy for both reactant heating and dissociation at 1773 K (545 and 678 kJ/mol for ZnO and SnO_2, respectively) and Q is the solar power entering the cavity. The neutral gas heating enthalpy was not taken into account. These data are listed in Table 2.

The typical thermochemical efficiency was 2%, which is similar to the one reported for a 10 kW reactor (1.1%).[15] Typical $\overline{f_{\text{mol}}}$ were 20% and 36% for ZnO and SnO_2 dissociations, respectively. This parameter was also estimated via an O_2 mole balance over the solar reactor[10]:

$$\overline{f_{\text{mol}}} = \frac{2n_{O_2}}{\Delta n_{\text{ox}}} \tag{11}$$

where the amount of O_2 at the reactor outlet (n_{O2}) is estimated by numerical integration of the O_2 signal over the solar test duration and Δn_{ox} by the oxide pellet variation. As an example, applying this method with the data from test #16 gave a value of 29% vs. 34% from Table 2. This moderate gap can be explained by the experimental uncertainties and it confirms that the measurements are physically consistent. Consequently, the O_2 signal was considered for an extended kinetic analysis. For ZnO dissociation, the reaction was shown to follow an ablation model in which the dissociation occurs more rapidly than the heat conduction in the ZnO irradiated layer.[27] Consequently, the reaction is surface-limited and the mass flow-rate of Zn released is,

$$F_{\text{red}} \cdot M_{\text{red}} = S_{\text{irr}} \cdot A_0 \exp\left(-\frac{E_a}{RT}\right) \tag{12}$$

where F_{red} denotes the instantaneous molar flow-rate of reduced species.

At the beginning of the dissociation reaction, the O_2 concentration (only traces) and the reduced species deposit are assumed small enough to neglect the parasitic heterogeneous recombination reaction. Consequently, the O_2 mole fraction, y_{O2}, can be expressed as:

$$y_{O_2} = \frac{2 \cdot A_0 \cdot S_{\text{irr}}}{M_{\text{red}} \cdot F_{\text{tot}}} \exp\left(-\frac{E_a}{RT}\right) \tag{13}$$

The irradiated reactant surface S_{irr} was assumed to lie between the section of the feeding tube (V, i.e. 10-mm-diameter) and the section of a sintered ZnO pellet after solar heating (Figure 10, 6-mm-diameter). Hence, a logarithmic regression was applied to estimate the kinetic parameters (Figure 11). This kinetic analysis was restricted to the initial step of the dissociation reaction (roughly 2–3 min.) corresponding to the start of the O_2 concentration increase (Figure 6) during the heating period from 1663 K. The estimated activation energy and pre-exponential factor for the ZnO dissociation were found to be 380 ± 16 kJ/mol and (20 ± 10) × 10^6 kg m^{-2} s^{-1}, respectively. These values are consistent with the ones obtained in a solar-driven thermogravimeter with a packed-bed of ZnO particles [E_a = 361 ± 53 kJ/mol, A_0 = (14.06 ± 2.73) × 10^6 kg m^{-2} s^{-1}].[27] This good agreement confirms that the surface reaction model (ablative mode) is suitable for the dissociation of ZnO shaped as a compressed rod.

Unlike ZnO case, powder sintering was not evidenced for SnO_2 after the solar test. Hence, the thermal dissociation of compressed SnO_2 pellet should rather be modeled by a reaction occurring in the material bulk and not only limited to the irradiated surface. Consequently, the ablation model is not suitable in the case of SnO_2 dissociation since an underlying layer reacts according to the temperature profile that settles during the moving-up and consumption of the SnO_2 rod.

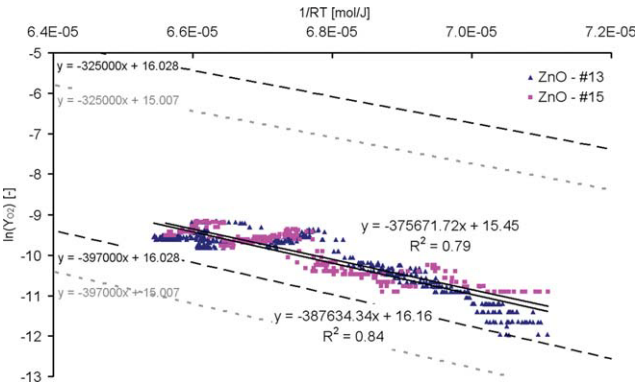

Figure 11. Logarithms of the O_2 mole fraction at the filter output relative to $1/RT_{pyro}$ for runs #13 and #15.

The data are framed by the ones inferred from previous kinetic data for ZnO dissociation[27]: A_0 = 14.06 × 10^6 kg m^{-2} s^{-1} and two activation energies corresponding to 95 or 105% of E_a = 361 kJ/mol. Dot for a 6 mm-diameter irradiated pellet surface, dash for a 10 mm-diameter one. [Color figure can be viewed in the online issue, which is available at wileyonlinelibrary.com.]

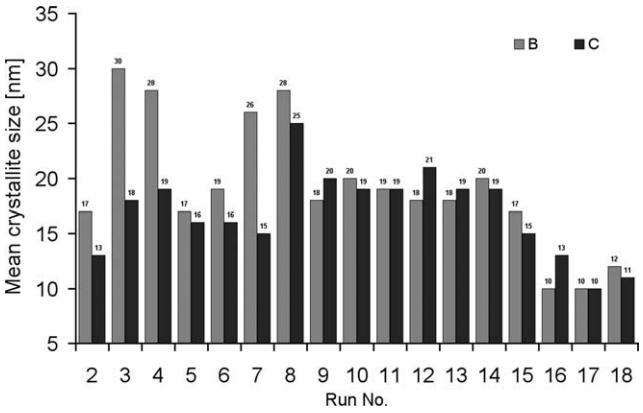

Figure 12. Mean crystallite diameter of the powders collected in zones B and C (filter) at the reactor output.

Morphological characterization of solar-produced powders

The typical mean crystallite size of the powders (deposits B and C) was estimated via XRD analysis and Scherrer's equation, and was found to be 20 and 10 nm for ZnO and SnO_2 dissociations, respectively (Figure 12). This was confirmed by scanning electron microscopy, showing micronic agglomerates of nanoparticles similar to those observed in,[28] with nanoentities typically below 30 nm (Figure 13). The size of the synthesized SnO particles was typically smaller compared to Zn.

Assuming spherical crystallites and negligible sintering between the surfaces, the specific surface area A_s was estimated from:

$$As = \frac{6}{d_c \rho} \tag{14}$$

where d_c is the mean crystallite diameter and ρ the reduced species density. The maximum specific surface area was thus about 50 and 60 m^2/g for Zn and SnO solar-produced powders, respectively. BET specific surface area measurements (manometric N_2 adsorption/desorption) showed that these powders are mesoporous (high porosity[28]) and have very high specific surface areas. For the deposit B powders, 17 ± 1 m^2/g and 41 ± 1 m^2/g were measured for Zn and SnO, respectively. For deposit C powders (collected on the filter), 19 ± 1 and 64 ± 1 m^2/g were obtained for Zn and SnO, respectively. Consequently, the incidence of sintering was relatively low, especially in the case of tin oxide. As a comparison, the powders studied in[28] were also analyzed and specific surface area of 21 ± 1 and 37 ± 1 m^2/g were measured for Zn and SnO, respectively. Hence, the specific surface area is weakly affected by a significant dilution ratio decrease (d in the range 200–1000 in[28]). According to these relatively high surface areas, the powders produced with this solar reactor are expected to show favorable hydrolysis kinetics, as observed in Ref. 28.

Conclusion

A novel lab-scale solar reactor was tested and qualified for ZnO and SnO_2 thermal dissociations in a controlled atmosphere at reduced pressure. This reactor, operating continuously and based on standard refractory materials (pure sintered alumina and alumino-silicate insulation), sustained repeated solar tests without significant cavity material degradations for an equilibrium temperature of about 1900 K. Each test produced about 1 g of powder with significant fractions of reduced species in less than half an hour for a pressure of 20 kPa and a minimum dilution ratio of 36. Its typical average thermochemical efficiency (1–3% range) over the experiment duration was consistent with the one expected for small-scale reactors. The high specific surface area of the recovered powders lets expect favorable kinetics for the subsequent water-splitting step. Online O_2 measurements were performed to determine the kinetics of the dissociation reaction. The obtained kinetic parameters for ZnO dissociation based on a surface reaction were in agreement with previous studies, whereas SnO_2 dissociation follows a different kinetic mechanism with a possible participation of the bulk material due to negligible sintering. Finally, the quenching device must be optimized in a future design via turbulent injection of neutral gas at the reactor output to improve both the yield of particle recovery and the mole fraction of reduced species in the produced powder.

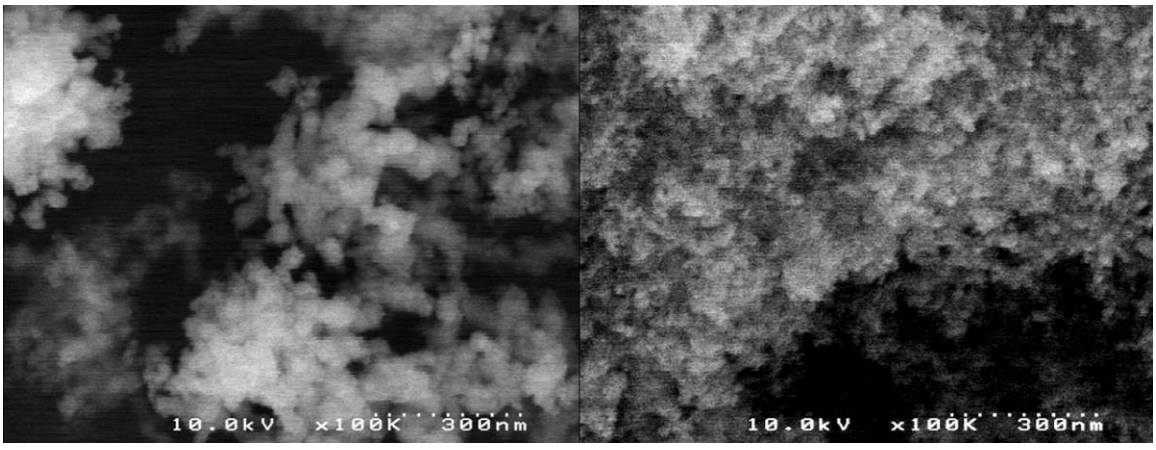

Figure 13. SEM photographs of solar-produced Zn (left) and SnO (right).

Acknowledgments

This study was supported by the CNRS and the Languedoc-Roussillon Regional Council. The Energy program of CNRS (DISCO2 project) and ANR (contract ANR-09-JCJC-0004-01) are also acknowledged for financial support. Authors gratefully acknowledge A. Julbe and J. Motuzas from IEM (Montpellier, France) for morphological characterizations, R. Garcia for the construction of the reactor and A. Soligo for technical assistance during solar tests.

Notation

A_0 = pre-exponential factor of the dissociation reaction (kg m^{-2} s^{-1})
A_s = specific surface area (m^2/kg)
B = constant inversely proportional to the residence time (S.I.)
C = solar concentration ratio of the parabola
d = dilution ratio
d_c = mean crystallite diameter (m)
E_a = activation energy of the dissociation reaction (J/mol)
F_i = molar flow-rate of compound i (mol/s)
F_{ng} = molar flow-rate of neutral gas (mol/s)
F_{tot} = total molar flow-rate at the reactor output (mol/s)
f_{mol} = mole fraction of reduced species in the solar-produced powder (mol %)
f_{wt} = mass fraction of reduced species in the solar-produced powder (wt %)
ΔH = enthalpy for the dissociation, including the reactant heating (J/mol)
L = oxide rod elevation (m)
M_i = molar weight of compound i (kg/mol)
m_p = total mass of products (kg)
m_i = mass of the reactants or of the products (kg)
m_c = mass of powder collected on the filter (kg)
Δm_{ox} = pellet mass variation (kg)
n_i = amount of compound i (mol)
Δn_{ox} = mole variation of the oxide pellet during thermal dissociation (mol)
npd = normalized pressure drop (m^2/kg)
P, P_i = total pressure or partial pressure of compound i (Pa)
ΔP = pressure variation during the solar test (Pa)
Q = incident power (W)
R = ideal gas constant (8.314 J/K/mol)
S = surface of the filter (m^2)
S_{irr} = irradiated reactant surface (m^2)
Δt = duration of the dissociation (s)
w_n = mass fraction of deposit n (n A, B or C)
y_{O2} = mole fraction of O_2 at the filter output

Greek letters

η = thermochemical efficiency
ρ = density (kg/m^3)

Literature Cited

1. Funk JE, Reinstrom RM. Energy requirements in the production of hydrogen from water. *Ind Eng Chem Process Des Dev*. 1966;5:336–342.
2. Steinfeld A. Solar hydrogen production via a two-step water-splitting thermochemical cycle based on Zn/ZnO redox reactions. *Int J Hydrogen Energy*. 2002;27:611–619.
3. Mills D. Advances in solar thermal electricity technology. *Solar Energy*. 2004;76:19–31.
4. Steinfeld A. Solar thermochemical production of hydrogen—a review. *Solar Energy*. 2005;78:603–615.
5. Perkins C, Weimer AW. Likely near-term solar-thermal water splitting technologies. *Int J Hydrogen Energy*. 2004;29:1587–1599.
6. Rosen MA. Advances in hydrogen production by thermochemical water decomposition: a review. *Energy*. 2010;35:1068–1076.
7. Bilgen E, Bilgen C. Solar hydrogen production using two-step thermochemical cycles. *Int J Hydrogen Energy*. 1981;7:637–644.
8. Palumbo R, Lédé J, Boutin O, Elorza-Ricart E, Steinfeld A, Möller S, Weidenkaff A, Fletcher EA, Bielicki E. The production of Zn from ZnO in a high-temperature solar decomposition quench process. I. The scientific framework for the process. *Chem Eng Sci*. 1998;53:2503–2517.
9. Vishnevetsky I, Epstein M. Production of hydrogen from solar zinc in steam atmosphere. *Int J Hydrogen Energy*. 2007;32:2791–2802.
10. Gstoehl D, Brambilla A, Schunk LO, Steinfeld A. A quenching apparatus for the gaseous products of the solar dissociation of ZnO. *React Solids*. 2008;43:4729–4736.
11. Abanades S, Charvin P, Lemort F, Flamant G. Novel two-step SnO_2/SnO water-splitting cycle for solar thermochemical production of hydrogen. *Int J Hydrogen Energy*. 2008;33:6021–6030.
12. Kang KS, Kim CH, Cho WC, Bae KK, Kim SH, Park CS. Novel two-step thermochemical cycle for hydrogen production from water using germanium oxide: KIER 4 thermochemical cycle. *Int J Hydrogen Energy*. 2009;34:4283–4290.
13. Müller R, Haeberling P, Palumbo R. Further advances toward the development of a direct heating solar thermal chemical reactor for the thermal dissociation of ZnO(s). *Solar Energy*. 2006;80:500–511.
14. Schunk LO, Haeberling P, Wepf S, Wuilllemin D, Meier A. A receiver-reactor for the solar thermal dissociation of zinc oxide. *ASME J Solar Energy Eng*. 2008;130:021009–1.
15. Schunk LO, Lipinski W, Steinfeld A. Heat transfer model of a solar receiver-reactor for the thermal dissociation of ZnO—Experimental validation at 10 kW and scale-up to 1 MW. *Chem Eng J*. 2009;150:502–508.
16. Haussener S, Hirsch D, Perkins C, Weimer A, Lewandowski A, Steinfeld A. Modeling of a multitube high-temperature solar thermochemical reactor for hydrogen production. *Solar Energy Eng*. 2009;131:24503.
17. Kodama T. High-temperature solar chemistry for converting solar heat to chemical fuels. *Prog Energy Combust Sci*. 2003;29:567–597.
18. Perkins C, Lichty P, Weimer AW, Bingham C. Fluid-wall effectiveness for preventing oxidation in solar-thermal ZnO reactors. *AIChE J*. 2007;53:1830–1844.
19. Chambon M, Abanades S, Flamant G. Design of a lab-scale rotary cavity-type solar reactor for continuous thermal dissociation of volatile oxides under reduced pressure. *ASME J Solar Energy Eng*. 2010;132:021006.
20. Charvin P, Abanades S, Lemort F, Flamant G. Analysis of solar chemical processes for hydrogen production from water splitting thermochemical cycles. *Energy Convers Manage*. 2008;49:1547–1556.
21. Abanades S, Charvin P, Flamant G. Design and simulation of a solar chemical reactor for the thermal reduction of metal oxides: case study of zinc oxide dissociation. *Chem Eng Sci*. 2007;62:6323–6333.
22. Perkins C, Lichty P, Weimer AW. Determination of aerosol kinetics of thermal ZnO dissociation by thermogravimetry. *Chem Eng Sci*. 2007;62:5952–5962.
23. Hagemann HJ, Gudat W, Kunz C. Optical constants from the far infrared to the X-ray region: Mg, Al, Cu, Ag, Au, Bi, C and Al_2O_3. *J Opt Soc Am*. 1975;65:742–744.
24. Jenkins R, Snyder R. *Introduction to X-ray Powder Diffractometry*. New York: Wiley, 1996.
25. Chambon M, Abanades S, Flamant G. Solar thermal reduction of ZnO and SnO_2: characterization of the recombination reaction with O_2. *Chem Eng Sci*. 2010;65:3671–3680.
26. Kouam J, Ait-Ahcene T, Plaiasu AG, Abrudeanu M, Motoc A, Beche E, Monty C. Characterization and properties of ZnO based nanopowders prepared by solar physical vapor deposition (SPVD). *Solar Energy*. 2008;82:226–238.
27. Schunk L, Steinfeld A. Kinetics of the thermal dissociation of ZnO exposed to concentrated solar irradiation using a solar-driven thermogravimeter in the 1800–2100 K range. *AIChE J*. 2009;55: 1497–1504.
28. Chambon M, Abanades S, Flamant G. Kinetic investigation of hydrogen generation from hydrolysis of SnO and Zn solar nanopowders. *Int J Hydrogen Energy*. 2009;34:5326–5336.

Manuscript received Jun. 18, 2010, and revision received Sept. 6, 2010.